

Lasing at the K -points of a honeycomb plasmonic lattice

R. Guo¹, M. Nečada¹, T.K. Hakala^{1,2}, A.I. Väkeväinen¹, and P. Törmä^{1*}

¹*Department of Applied Physics, Aalto University, FI-00076 Aalto, Finland*

²*Institute of Photonics, University of Eastern Finland, P.O. Box 111, FI-80101 Joensuu, Finland*

We study lasing at the high-symmetry points of the Brillouin zone in a honeycomb plasmonic lattice. We use symmetry arguments to define singlet and doublet modes at the K -points of the reciprocal space. We experimentally demonstrate lasing at the K -points that is based on plasmonic lattice modes and two-dimensional feedback. By comparing polarization properties to T -matrix simulations, we identify the lasing mode as one of the singlets with an energy minimum at the K -point enabling feedback. Our results offer prospects for studies of topological lasing in radiatively coupled systems.

Feedback provided by a resonator is essential for lasing. The resonator can be a set of mirrors [1] or periodic structures enabling distributed feedback (DFB) lasing [2–6]. Most DFB lasers rely on simple one-dimensional periodic structures. More complex geometries would offer such interesting features as distributed feedback involving multiple modes, flat bands, and increased variety of degenerate high-symmetry points and possibilities of creating topological bands [7]. The symmetry of a hexagonal Bravais lattice leads to the possibility to multiply degenerate points at the first Brillouin zone edge [3]. Here we experimentally demonstrate lasing at K -points of a honeycomb plasmonic lattice.

The vast majority of the work on bosons in hexagonal/honeycomb lattices, for photonic [9–11], microwave [12, 13], and atomic [14–17] systems realize essentially the tight-binding model of the lattice. That is, the lattice sites are connected only up to the (next-)nearest neighbor; in the optical systems, this is realized by site-to-site near-field coupling. Our system consists of an array of plasmonic nanoparticles that are radiatively coupled over the whole system size. This renders tight-binding models useless, and we base our theoretical description on symmetry arguments and T -matrix scattering simulations.

Plasmonic nanohole and nanoparticle arrays combined with organic and inorganic gain materials are emerging as a versatile platform for room-temperature, ultrafast lasing [18–32] and Bose-Einstein condensation [2, 33]. These works, however, focus on lasing action or condensation at the Γ -point, that is, at the center of the Brillouin zone of systems with a Bravais lattice that is rectangular/square [18–22, 24–27, 29], hexagonal [30, 32] or one-dimensional [28] (ref. [31] studies lasing action in the X -point of a square lattice).

K -point lasing or condensation in radiatively (long-range) coupled hexagonal/triangular lattices has been studied in photonic crystal [35–37] and exciton-polariton [38] systems. In those works, however, the polarization properties of the output light were not analyzed. Here we demonstrate lasing at the K -points and show that the polarization properties and real-space pat-

terns of the laser emission contain essential information about the lasing mode. We identify the lasing mode as one of the singlets allowed by symmetry and explain why this mode is selected by the lasing action.

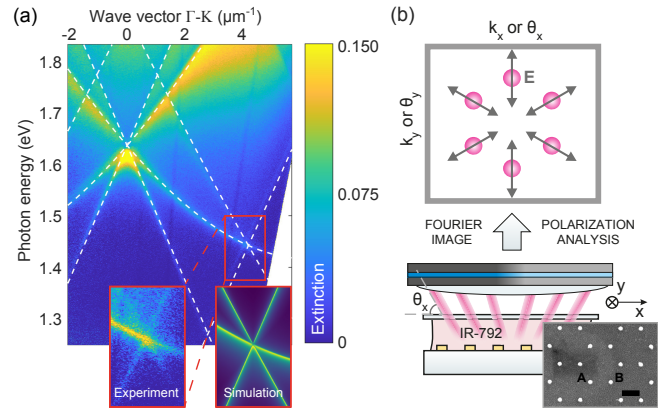


Figure 1. (a) A measured angle-resolved extinction spectrum of a honeycomb lattice with particle separation of $p = 576$ nm. Color scale shows the extinction which is defined as $(1 - \text{normalized transmission})$. The SLR modes correspond to extinction maxima, closely following the diffracted orders (dashed lines). The left inset shows the measured dispersion around the K -point (the color scale is from 0 to 0.05). The right inset shows the dispersion obtained by T -matrix simulations. (b) The lasing measurements. Nanoparticle samples combined with IR-792 molecules in solution are pumped with a femtosecond laser. The hexagonal geometry of the lattice (inset: scanning electron microscope image of the gold nanoparticles, scale bar 500 nm, with the A and B unit cell sites marked) enables lasing emission in six distinct off-normal angles, collected by a 0.6 NA objective and further analyzed. In the Fourier image, the six angles correspond to lasing at the six K -points of the first Brillouin zone, with distinct polarization directions (grey arrows) of the electric field \mathbf{E} .

We fabricate cylindrical gold nanoparticles with electron-beam lithography on a glass substrate in a honeycomb lattice arrangement. The particle separation is varied between 569–583 nm. Individual nanoparticles have a nominal diameter of 100 nm and height of 50 nm. An organic dye molecule IR-792 is added on top of the array in 25 mM solution and the structure is sealed with a glass superstrate (Fig. 1(b)). The dye molecules act as

* paivi.torma@aalto.fi

the gain material and are optically pumped with 100 fs laser pulses (750 nm central wavelength). For details, see section I of Supplemental Material.

The energies of diffracted orders (DOs) of a 2D hexagonal lattice are shown with dashed lines in Fig. 1(a) for the Γ - K in-plane (x - y plane) momentum direction. The DOs correspond to diffraction without resonant phenomena at the lattice sites, so-called empty lattice approximation. In our samples, the nanoparticles have a broad plasmonic resonance (at 1.87 eV, width ~ 300 meV) which hybridizes with the DOs, leading to narrow (width 5–20 meV) dispersive modes called surface lattice resonances (SLRs) [39, 40], Fig. 1(a). A dispersion obtained by multiple-scattering T -matrix simulation (for details, see [24] and section IV of supplemental Material) agrees with the experiments, see the insets of Fig. 1(a). The dispersions are measured with a Fourier imaging setup used in our previous works [2, 24, 41] but now extended to larger angles.

The geometry of an infinite honeycomb lattice belongs to the group $p6m \times \sigma_h$, the wallpaper group $p6m$ [42] extended by the horizontal reflection σ_h . The horizontal reflection ensures that the eigenmodes can be divided into two classes according to the electric field orientation at the mirror plane: the electric field \mathbf{E} is either parallel (in-plane- \mathbf{E} , the magnetic field \mathbf{H} is then perpendicular to the mirror plane) or perpendicular (perpendicular- \mathbf{E} , magnetic field \mathbf{H} in-plane) [3].

A single unit cell of the reciprocal lattice of our system contains six high symmetry points (Fig. 2(d)): one Γ -point with D_6 point symmetry, as well as two K -points with D_3 and three M -points with D_2 point symmetries. The K -points are mutually related by parity inversion symmetry. Whenever the distinction between the two K -points is relevant, we label the other one as K' . To a large extent, group theory determines the properties of the eigenmodes supported at the high-symmetry points. As the reciprocal lattice has D_3 point group symmetry around the K -points, the K -point modes must constitute irreducible representations of the D_3 group. Using standard group-theoretical reduction methods [4], we can determine for instance the electric dipole polarizations of the nanoparticles in the respective modes. The irreducible representations of D_3 are either one- or two-dimensional, so the eigenmodes are, apart from accidental degeneracies, either non-degenerate (“singlets”, 1D representation) or doubly degenerate (“doublets”, 2D representation). Six dispersion branches meet at the K -point (see section II of Supplemental Material), and the eigenmodes constitute two singlets and two doublets.

Fig. 2(a) shows the admissible patterns of nontrivial nanoparticle dipole polarizations in the in-plane- \mathbf{E} case for the singlets and one doublet. Any linear combination of the depicted doublet states is possible as well. Fig. 2(b) shows spatial Fourier transforms of these patterns, corresponding to the polarizations of the far-field beams escaping the array.

In real space, the magenta color in Fig. 2 means clock-

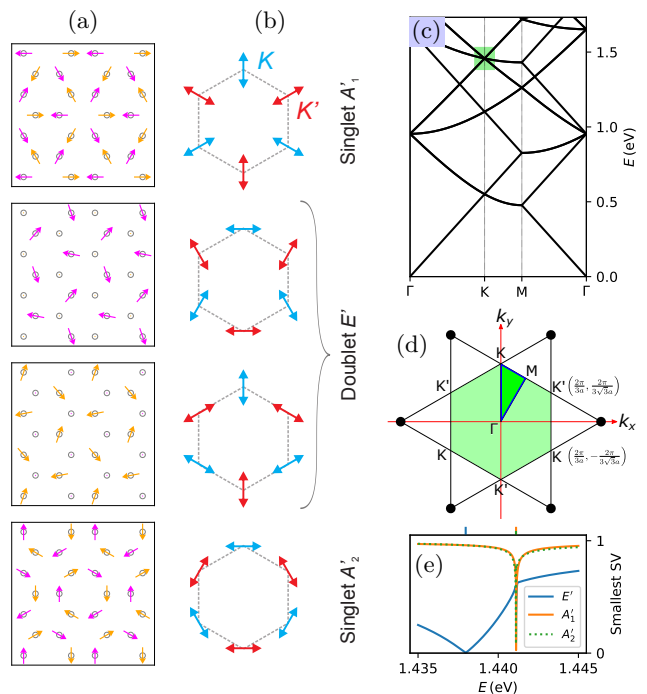


Figure 2. Eigenmodes of the honeycomb plasmonic lattice at the K -point. (a) Real-space electric dipole polarizations of the nanoparticles (circles) corresponding to two singlet modes and a doublet mode, at a specific time. The dipole polarizations depicted by orange and magenta arrows evolve in time rotating clockwise and counterclockwise, respectively, for the K mode, and in the opposite directions for the K' mode. (b) Fourier transform of the dipole polarizations in the corresponding eigenmodes. (c) Band structure of the empty lattice model, that is, as given by diffracted orders of a periodic structure without the effect of the localized plasmonic resonance of the nanoparticles, with the studied K -point highlighted. (d) The first Brillouin zone (green area) of the honeycomb reciprocal lattice and its high symmetry points, a is the lattice constant. (e) Singular values (SV) of the symmetry-adapted scattering problem at the K -point, whose minima give the mode energies, as function of energy. The color shows the results of projection of the corresponding eigenmodes on the singlets and doublets obtained by group theory (the singlet A_1' that was found to lase experimentally is shown in orange, the other singlet A_2' in green, and the doublet E' in blue), the energies are marked by ticks.

wise rotating electric dipole polarizations while orange means the dipoles rotate counterclockwise for all K -modes. For K' -modes, the polarization rotation directions are reversed. If the system is excited simultaneously in the K and corresponding K' states with the same intensities, the polarizations will, instead of rotating, oscillate in a linear direction, with the exact direction depending on the relative phase between the K and K' modes. This will be important in analyzing the experimental real-space images.

To characterize the lasing action, we perform angle, energy, polarization and position resolved emission measurements. Above a critical pump threshold, the sample

exhibits an intense and narrow emission peak at 1.426 eV and $k_y \sim 4.25 \times 10^6 \text{ m}^{-1}$ (corresponding to an angle of $35^\circ \pm 0.4^\circ$ with respect to the sample normal), see Fig. 3(a-c). The emission intensity and mode line width as a function of pump fluence is shown in Fig. 3(b). Over three orders of magnitude increase in emission intensity can be seen upon the onset of lasing, typical for nanoparticle arrays with small spontaneous emission coupling to the lasing mode (small β -factor [44]) [24, 26, 28, 29, 31]. Increased temporal coherence due to lasing is evident from the line width of the emission (2 meV), which is well below the natural line width of the SLR mode at the K -point ($\sim 20 \text{ meV}$). The 2 meV line width is smaller than those in [18, 21, 22, 26, 31, 32] (3.6–27 meV), but larger than the values 0.26–1.5 meV in [20, 24, 25, 28, 29].

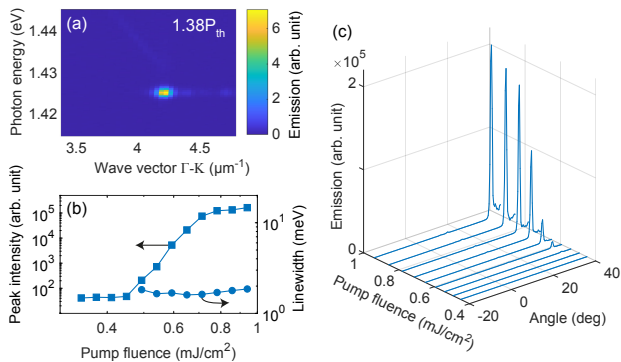


Figure 3. (a) Measured emission spectra of a honeycomb lattice with $P = 1.38P_{\text{th}}$, where $P_{\text{th}} = 0.47 \text{ mJ}/\text{cm}^2$ is the threshold pump fluence for the K -point lasing mode (particle distance $p = 576 \text{ nm}$ and diameter $d = 100 \text{ nm}$). (b) The mode output power (squares) and the line width (circles) at the K -point angle ($35^\circ \pm 0.4^\circ$) as a function of pump fluence. Note that due to low intensity, we cannot determine the line width at pump fluences below the threshold, for below threshold emission, see Fig. S5 in Supplemental Material. (c) The emission intensity as a function of angle at the K -point energy ($\sim 1.426 \text{ eV}$) with several pump fluences.

In Fig. 4(a), we show the angle resolved emission of the sample. The system exhibits lasing at six specific angles that correspond to three K and three K' points of the lattice. We measure the polarization properties of each point by recording the emission intensities with several different linear polarizer angles. For each point, we recover a typical dipolar emission pattern, however, the direction of linear polarization is different, see Fig. 4(b). The results match excellently the calculated angular distributions of linearly polarized light having a polarization along the six Γ - K directions (the red dashed lines). We find that the A'_1 singlet mode has corresponding polarization properties, see Fig. 2(b). The linear polarization degree $\rho_L = (I_{\text{max}} - I_{\text{min}})/(I_{\text{max}} + I_{\text{min}})$ has an average 0.8 for the six K -points.

The identification of the lasing mode as the singlet A'_1 can be further confirmed by analyzing the real-space

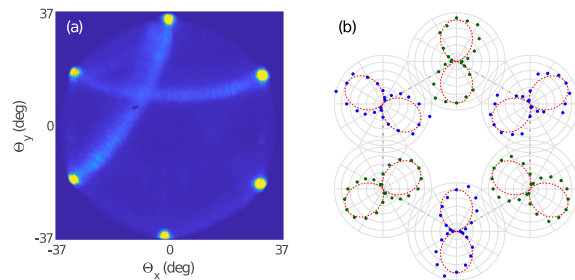


Figure 4. Lasing mode polarization. (a) Angle resolved emission of the sample without any polarizer in detection. All six K -points are clearly visible. (b) Polar emission intensities at each K -point in the presence of a linear polarizer. The angles refer to the polarizer angles and the radii refer to the measured intensities. The red dashed lines are the calculated intensity distributions for linearly polarized light (along the Γ - K directions) passing through the polarizer at the corresponding angle.

images with variously oriented polarization filters at the output. While the dipole polarization directions of the nanoparticles cannot be measured directly, we can estimate them using the spatial intensity variations due to wave interference in case of different filter orientations. The intensity variations should be most clear in the case where the system lases in the K and K' modes simultaneously, with a fixed (modulo $\pi/3$) relative phase such that the dipoles are oriented as in Fig. 2(a). If the system lases only in one of the K or K' modes, or if the relative phase is random, the real-space intensity distribution should become more uniform due to time averaging (see section III C of Supplemental Material).

Fig. 5 shows an image of a small piece of the array for three choices of polarization filters for the lasing emission, with the predicted intensities and nanoparticle electric dipole polarizations of the singlet mode A'_1 for the ideal, namely zero phase-difference combination of the K and K' modes, as defined in Fig. 2(a) (cases with other polarization filter orientations and details of the theoretical predictions are shown in section III of Supplemental Material). The intensity maxima appear at the places where the surrounding adjacent dipoles, or their projections according to the polarization filter orientation, have the same or similar directions and therefore interfere constructively. Comparing the real-space images with dipole orientations predicted for the other modes (A'_2 and the doublet E') results in inconsistencies (for details, see Supplemental Material, section III). This confirms that the system indeed lases in the singlet mode A'_1 . The intensity variations in the observed patterns show that the system lases in the K and K' singlet A'_1 modes simultaneously, with comparable intensities and with a fixed, or at least strongly correlated, relative phase. The existence of interference patterns over the whole sample, furthermore, proves the spatial coherence of the observed lasing. Since the K -point of our system corresponds to the crossing of diffractive orders in three directions with 120° angles

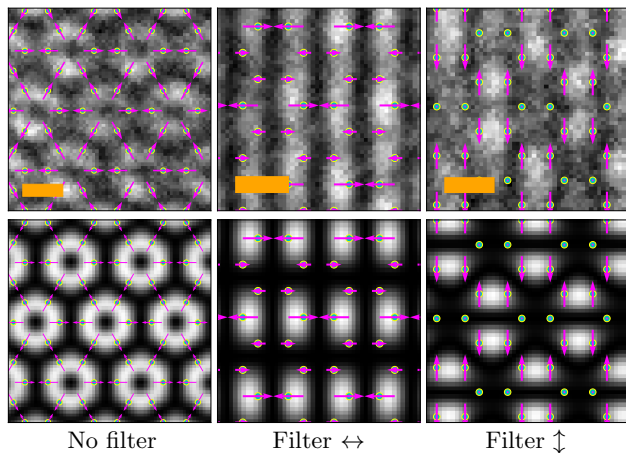


Figure 5. Upper row: examples of real-space images for different polarization filters (no filter, horizontal, vertical) used for the analysis of the lasing mode. In each case, the expected positions of the nanoparticles (small yellow-cyan circles) and the dipole polarizations (arrows) of the singlet mode A'_1 for the ideal (zero) $K-K'$ relative phase are depicted, projected to the corresponding filter direction. Lower row: theoretical prediction for the intensities for the ideal $K-K'$ relative phase. The scale bar length is $1\ \mu\text{m}$. For images over larger areas, see section III of Supplemental Material.

between them, the feedback in the lasing action is two dimensional, different from one dimensional DFB lasing [2] in nanoparticle arrays [24, 25, 28, 45]. This is reflected in the non-trivial 2D polarization patterns.

DFB-type lasing typically occurs at a band edge or an extremum of the dispersion because zero group velocity enables feedback. Both the measured and simulated dispersions (Fig. 1(a)) show crossings of the modes at the K -point, without any visible gap and zero group velocity point. Why does a mode of a certain symmetry (the A'_1 singlet) lase, if the K -point apparently has a degeneracy of several modes? To answer this we computed the energies of the eigenmodes using symmetry-adapted T -matrix simulations (for details, see sections IV–V of Supplemental Material). Fig. 2(e) shows that indeed there is a difference in the energies of the A'_1 singlet and the E' doublet near the K -point. This band gap means that the singlet A'_1 has an energy minimum at the K -point, which explains why lasing is possible in this mode. The narrower peak for A'_1 compared to that for E' indicates higher quality factor, making the former mode more amenable for lasing. The A'_2 singlet mode seems almost degenerate with A'_1 but the resonance is a bit weaker (slightly smaller dip in Fig. 2(e); see Fig. S11 of Supplemental Material for a larger picture) The energy difference between A'_1 and E' is only 3.2 meV, smaller than the natural linewidth of the SLR mode around 20 meV, which explains why the gap is not visible in the dispersions. On the other hand, the lasing emission has

2 meV linewidth, similar to the scale of the band gap.

In summary, we have observed lasing action at the K and K' points of a honeycomb plasmonic lattice. Both the polarization of the six output beams and the real space interference patterns provide distinct features that, when combined with the group theory description, reveal the lasing mode as the singlet A'_1 . Analysis of the T -matrix simulation results using the group theory eigenmodes showed that the singlet A'_1 has an energy minimum at the K -point, which enables the feedback necessary for lasing. Our results demonstrate the potential of plasmonic nanoparticle array systems for tailoring the polarization and beam direction of laser output by the lattice geometry. The tunability of the beam direction (here $\sim 35^\circ$) can be used for bringing the beam close to the in-plane direction. If realized in a less lossy platform, this could enable on-chip planar integration.

Our study gives a promising starting point for investigations of topological photonics and lasing [7, 46–53] in radiatively coupled systems. Plasmonic nanoparticle array lasers offer a unique combination of easy fabrication, room temperature operation, ultrafast speeds, long-range radiative coupling, and strong coupling to emitters (the gain medium) [26, 54, 55]. Radiatively coupled systems offer topological phenomena different from tight-binding models [56]. Arrays of magnetic nanoparticles have been realized [57], and the magnetization of nanoparticles could be used for opening topological gaps at the high-symmetry points where we have shown lasing. Time reversal symmetry breaking is one of the main mechanisms leading to topologically non-trivial systems but topological gaps based on magnetic materials [52, 53] are extremely small at optical frequencies [46]. The polarization and interference analysis demonstrated here will be invaluable in identifying topological modes even when related gaps would be small. Remarkably, the lasing action is stable despite a small gap, which is promising concerning topological lasing relying on small topological gaps.

ACKNOWLEDGMENTS

This work was supported by the Academy of Finland through its Centres of Excellence Programme (Projects No. 284621, No. 303351, No. 307419) and by the European Research Council (Grant No. ERC-2013-AdG-340748-CODE). This work benefited from discussions and visits within the COST Action MP1403 Nanoscale Quantum Optics, supported by COST (European Cooperation in Science and Technology). Part of the research was performed at the Micronova Nanofabrication Centre, supported by Aalto University. Computing resources were provided by the Triton cluster at Aalto University. The authors thank Matthias Saba, Ortwin Hess, Tero Heikkilä and Heikki Rekola for fruitful discussions.

- [1] F. Koyama, S. Kinoshita, and K. Iga, *Appl. Phys. Lett.* **55**, 221 (1989).
- [2] H. Kogelnik and C. V. Shank, *J. Appl. Phys.* **43**, 2327 (1972).
- [3] J. P. Dowling, M. Scalora, M. J. Bloemer, and C. M. Bowden, *J. Appl. Phys.* **75**, 1896 (1994).
- [4] M. Meier, A. Mekis, A. Dodabalapur, A. Timko, R. E. Slusher, J. D. Joannopoulos, and O. Nalamasu, *Appl. Phys. Lett.* **74**, 7 (1998).
- [5] S. Noda, M. Yokoyama, M. Imada, A. Chutinan, and M. Mochizuki, *Science* **293**, 1123 (2001).
- [6] H. Matsubara, S. Yoshimoto, H. Saito, Y. Jianglin, Y. Tanaka, and S. Noda, *Science* **319**, 445 (2008).
- [7] T. Ozawa, H. M. Price, A. Amo, N. Goldman, M. Hafezi, L. Lu, M. Rechtsman, D. Schuster, J. Simon, O. Zilberberg, and I. Carusotto, arXiv: 1802.04173 (2018).
- [8] M. S. Dresselhaus, G. Dresselhaus, and A. Jorio, *Group Theory: Application to the Physics of Condensed Matter* (Springer, Berlin, Heidelberg, 2008).
- [9] G. Weick, C. Woollacott, W. L. Barnes, O. Hess, and E. Mariani, *Phys. Rev. Lett.* **110**, 106801 (2013).
- [10] M. C. Rechtsman, J. M. Zeuner, Y. Plotnik, Y. Lumer, D. Podolsky, F. Dreisow, S. Nolte, M. Segev, and A. Szameit, *Nature* **496**, 196 (2013).
- [11] T. Jacqmin, I. Carusotto, I. Sagnes, M. Abbarchi, D. D. Solnyshkov, G. Malpuech, E. Galopin, A. Lemaitre, J. Bloch, and A. Amo, *Phys. Rev. Lett.* **112**, 116402 (2014).
- [12] S. Bittner, B. Dietz, M. Miski-Oglu, P. Oria Iriarte, A. Richter, and F. Schäfer, *Phys. Rev. B* **82**, 014301 (2010).
- [13] M. Bellec, U. Kuhl, G. Montambaux, and F. Mortessagne, *Phys. Rev. Lett.* **110**, 033902 (2013).
- [14] C. Becker, P. Soltan-Panahi, J. Kronjäger, S. Dörscher, K. Bongs, and K. Sengstock, *New J. Phys.* **12**, 065025 (2010).
- [15] Z. Chen and B. Wu, *Phys. Rev. Lett.* **107**, 065301 (2011).
- [16] J. Struck, M. Weinberg, C. Ölschläger, P. Windpassinger, J. Simonet, K. Sengstock, R. Höppner, P. Hauke, A. Eckardt, M. Lewenstein, and L. Mathey, *Nat. Phys.* **9**, 738 (2013).
- [17] T. Li, L. Duca, M. Reitter, F. Grusdt, E. Demler, M. Endres, M. Schleier-Smith, I. Bloch, and U. Schneider, *Science* **352**, 1094 (2016).
- [18] W. Zhou, M. Dridi, J. Y. Suh, C. H. Kim, D. T. Co, M. R. Wasielewski, G. C. Schatz, and T. W. Odom, *Nat. Nanotechnol.* **8**, 506 (2013).
- [19] F. van Beijnum, P. J. van Veldhoven, E. J. Geluk, M. J. A. de Dood, G. W. 't Hooft, and M. P. van Exter, *Phys. Rev. Lett.* **110**, 206802 (2013).
- [20] X. Meng, J. Liu, A. V. Kildishev, and V. M. Shalaev, *Laser Photon. Rev.* **8**, 896 (2014).
- [21] A. H. Schokker and A. F. Koenderink, *Phys. Rev. B* **90**, 155452 (2014).
- [22] A. Yang, T. B. Hoang, M. Dridi, C. Deeb, M. H. Mikkelsen, G. C. Schatz, and T. W. Odom, *Nat. Commun.* **6**, 6939 (2015).
- [23] J. Cuerda, F. Rüting, F. J. García-Vidal, and J. Bravo-Abad, *Phys. Rev. B* **91**, 041118 (2015).
- [24] T. K. Hakala, H. T. Rekola, A. I. Väkeväinen, J.-P. Martikainen, M. Nečada, A. J. Moilanen, and P. Törmä, *Nat. Commun.* **8**, 13687 (2017).
- [25] D. Wang, A. Yang, W. Wang, Y. Hua, R. D. Schaller, G. C. Schatz, and T. W. Odom, *Nat. Nanotechnol.* **12**, 889 (2017).
- [26] M. Ramezani, A. Halpin, A. I. Fernández-Domínguez, J. Feist, S. R.-K. Rodriguez, F. J. Garcia-Vidal, and J. G. Rivas, *Optica* **4**, 31 (2017).
- [27] A. H. Schokker, F. van Riggelen, Y. Hadad, A. Alù, and A. F. Koenderink, *Phys. Rev. B* **95**, 085409 (2017).
- [28] H. T. Rekola, T. K. Hakala, and P. Törmä, *ACS Photonics* **5**, 1822 (2018).
- [29] K. S. Daskalakis, A. I. Väkeväinen, J.-P. Martikainen, T. K. Hakala, and P. Törmä, *Nano Lett.* **18**, 2658 (2018).
- [30] V. T. Tenner, M. J. A. d. Dood, and M. P. v. Exter, *Opt. Lett.* **43**, 166 (2018).
- [31] H.-Y. Wu, L. Liu, M. Lu, and B. T. Cunningham, *Adv. Opt. Mater.* **4**, 708 (2016).
- [32] C. Zhang, Y. Lu, Y. Ni, M. Li, L. Mao, C. Liu, D. Zhang, H. Ming, and P. Wang, *Nano Lett.* **15**, 1382 (2015).
- [33] J.-P. Martikainen, M. O. J. Heikkinen, and P. Törmä, *Phys. Rev. A* **90**, 053604 (2014).
- [34] T. K. Hakala, A. J. Moilanen, A. I. Väkeväinen, R. Guo, J.-P. Martikainen, K. S. Daskalakis, H. T. Rekola, A. Julku, and P. Törmä, *Nat. Phys.* **14**, 739 (2018).
- [35] M. Notomi, H. Suzuki, and T. Tamamura, *Appl. Phys. Lett.* **78**, 1325 (2001).
- [36] S. W. Chen, T. C. Lu, Y. J. Hou, T. C. Liu, H. C. Kuo, and S. C. Wang, *Appl. Phys. Lett.* **96**, 071108 (2010).
- [37] W. Huang, D. Pu, W. Qiao, W. Wan, Y. Liu, Y. Ye, S. Wu, and L. Chen, *J. Phys. D: Appl. Phys.* **49**, 335103 (2016).
- [38] N. Y. Kim, K. Kusudo, A. Löffler, S. Höfling, A. Forchel, and Y. Yamamoto, *New J. Phys.* **15**, 035032 (2013).
- [39] S. Zou and G. C. Schatz, *Chem. Phys. Lett.* **403**, 62 (2005).
- [40] W. Wang, M. Ramezani, A. I. Väkeväinen, P. Törmä, J. G. Rivas, and T. W. Odom, *Materials Today* **21**, 303 (2018).
- [41] R. Guo, T. K. Hakala, and P. Törmä, *Phys. Rev. B* **95**, 155423 (2017).
- [42] T. Hahn, *International Tables for Crystallography, Vol. A: Space Group Symmetry*, 5th ed., IUCr Series. International Tables of Crystallography (Springer, Dordrecht, 2002).
- [43] J. D. Dixon, *Math. Comp.* **24**, 707 (1970).
- [44] G. Björk and Y. Yamamoto, *IEEE Journal of Quantum Electronics* **27**, 2386 (1991).
- [45] D. Wang, W. Wang, M. P. Knudson, G. C. Schatz, and T. W. Odom, *Chem. Rev.* **118**, 2865 (2017).
- [46] B. Bahari, A. Ndao, F. Vallini, A. E. Amili, Y. Fainman, and B. Kanté, *Science* **358**, 636 (2017).
- [47] A. B. Khanikaev and G. Shvets, *Nat. Photonics* **11**, 763 (2017).
- [48] G. Harari, M. A. Bandres, Y. Lumer, M. C. Rechtsman, Y. D. Chong, M. Khajavikhan, D. N. Christodoulides, and M. Segev, *Science* **359**, 1230 (2018).
- [49] M. A. Bandres, S. Wittek, G. Harari, M. Parto, J. Ren, M. Segev, D. N. Christodoulides, and M. Khajavikhan, *Science* **359**, 1231 (2018).
- [50] L. Lu, J. D. Joannopoulos, and M. Soljačić, *Nat. Photonics* **8**, 821 (2014).

- [51] L. Lu, J. D. Joannopoulos, and M. Soljačić, *Nat. Phys.* **12**, 626 (2016).
- [52] F. D. M. Haldane and S. Raghu, *Phys. Rev. Lett.* **100**, 013904 (2008).
- [53] S. Raghu and F. D. M. Haldane, *Phys. Rev. A* **78**, 033834 (2008).
- [54] A. I. Väkeväinen, R. J. Moerland, H. T. Rekola, A.-P. Eskelinen, J.-P. Martikainen, D.-H. Kim, and P. Törmä, *Nano Lett.* **14**, 1721 (2014).
- [55] P. Törmä and W. L. Barnes, *Rep. Prog. Phys.* **78**, 013901 (2015).
- [56] S. R. Poochock, X. Xiao, P. A. Huidobro, and V. Giannini, *ACS Photonics* **5**, 2271 (2018).
- [57] M. Kataja, T. K. Hakala, A. Julku, M. J. Huttunen, S. van Dijken, and P. Törmä, *Nat. Commun.* **6**, 7072 (2015).

Lasing at the K -points of a honeycomb plasmonic lattice

Supplemental Material

I. EXPERIMENTAL METHODS

A. Sample fabrication

Honeycomb lattices of cylindrical gold nanoparticles (diameter 100 nm, height 50 nm) were fabricated on borosilicate substrate with electron beam lithography (Vistec EPBG5000pES, acceleration voltage: 100kV). Two nanometers of titanium was deposited prior to gold deposition to provide an adhesive layer. The overall size of the array was $100 \times 100 \mu\text{m}^2$.

B. Gain medium

The gain medium used was dye IR-792 perchlorate purchased from Sigma-Aldrich. The dye molecule was dissolved into 1:2 (dimethyl sulfoxide):(benzyl alcohol) solvent with a concentration of 25 mM. Figure S1 shows the emission spectrum of the dye solvent with the same concentration. Amplified spontaneous emission and lasing of IR-792 have been reported previously in systems of dye-doped polymer thin film [S1] and of edge-pumped plasmonic lattice [S2].

C. Measurement setup

A schematic of the measurement setup is presented in Figure S2. The back focal plane of a 40×0.6 NA microscope objective was focused to the entrance slit of a spectrometer with a focal length of 500 mm and a spec-

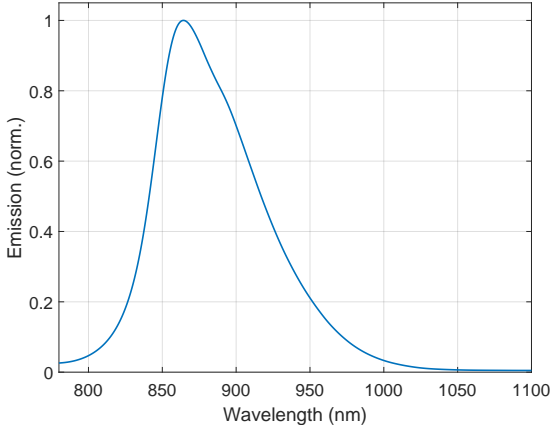


Figure S1. Measured emission spectrum of the IR-792 dye.

tral resolution of ~ 0.5 nm. The angle-resolved extinction spectra (the dispersion) were obtained by focusing light from a halogen lamp onto the sample. The sample substrate was placed in a 10° tilted stage in order to collect light asymmetrically from higher angles than the objective NA would allow at normal incidence. The measured spectra (namely, the images from the spectrometer CCD) were further calibrated by the diffraction pattern from a 300 lines/mm transmission grating. The metal nanoparticle array was fabricated on top of a glass substrate, and for the lasing measurement, a 1 mm thick dye (IR-792) solution layer (of volume $\sim 300 \mu\ell$) was added on top of the array. The solution layer was sealed between the glass substrate and a glass superstrate. The 1 mm dye solution layer on top of the array is much higher than the extension of the fields related to the nanoparticles, and also high enough not to create a waveguide mode at the wavenumbers considered. Therefore the exact alignment of the two glass slides with respect to each other is not essential. The dye solution was pumped with a femtosecond laser with $\sim 60^\circ$ incident angle, 750 nm central wavelength, 100 fs pulse width and 1 kHz repetition frequency at room temperature. The laser spot size on the sample is $\sim 4.4 \times 10^5 \mu\text{m}^2$. The real and back focal plane images of the lasing action were taken by focusing them onto two separate 2D CCD cameras. The polarizer used in the polarization measurements was Thorlabs nanoparticle linear film polarizer (model LPVIS100-MP2) which has an extinction ratio of $> 10^6 : 1$ in the wavelength range of interest.

D. Lasing results

Figure S3 shows a comparison of lasing threshold curves for the peak intensities and integrated intensities under the lasing peak. Figure S4 shows the data of Fig. 3(c) of the main text in double logarithmic scale. Figure S5 shows the measured emission spectrum below the threshold.

II. DIFFRACTION ORDERS AND NUMBER OF MODES

The diffraction orders, that is, the empty lattice calculation for our honeycomb array are shown in Fig. S6. The right panel is the same as shown in Fig. 2(c) of the main text. The left panel shows a crosscut at the K -point energy, from where one can see that six dispersion branches (in-plane polarized light cones) meet at the K -point. Correspondingly, there will also be six eigenmodes: two singlets and two doublets as following from

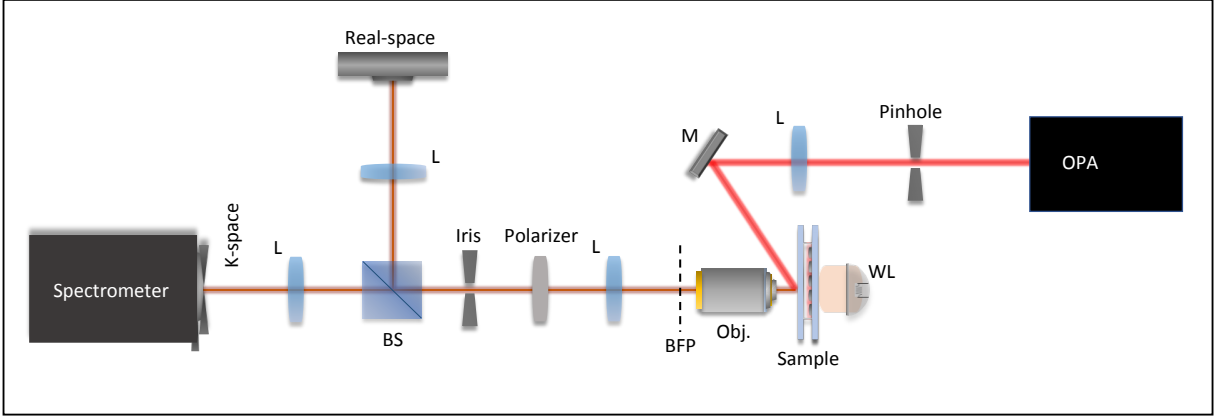


Figure S2. Measurement setup. L stands for lens, M for mirror, BS for beam splitter, BFP for back-focal plane, Obj. for objective, WL for white light source and OPA for optical parametric amplifier. The OPA is used to tune the pump wavelength, here we used 750 nm.

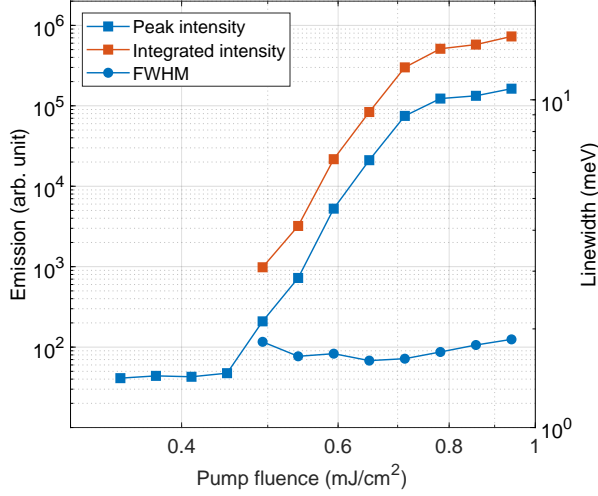


Figure S3. Comparison of the threshold curves with just the peak value (blue) and with integrated intensity under the lasing peak. Both show the same threshold behavior.

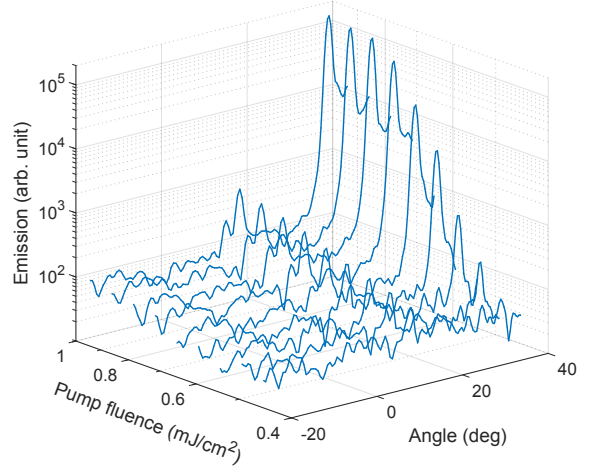


Figure S4. Data of the Figure 3(c) of the main text in double logarithmic scale.

decomposition of the vector space spanned by linearly combining plane waves (or dipole polarization degrees of freedom) into irreducible representations (subject to the D_3 symmetry of given K -point) [S3, S4].

For background refractive index 1.52 and 576 nm spacing between neighboring nanoparticle centers (i.e. 998 nm lattice period), the third crossing of diffraction orders at the K -point happens at energy 1.44 eV. The slight difference from the energy of 1.426 eV from Fig. 3 is most likely due to the real background index of refraction not having exactly the value of 1.52 used in the simulations.

III. DETERMINING THE LASING MODES IN REAL SPACE

In our experiment, the diameter of a single nanoparticle is much smaller than the wavelength, hence the nanoparticle can be considered as a monochromatic point source when lasing. Imaged with a sufficient resolution, such source will appear as a diffraction pattern rather than a dot. The exact profile of the pattern will depend on the actual optical setup, but for practical purposes of our real-space pattern analysis, it can be modeled as an Airy pattern. In such case, the source s will create

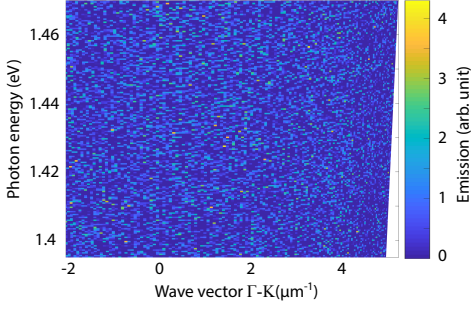


Figure S5. Measured emission spectrum below the threshold ($P = 0.75P_{\text{th}}$).

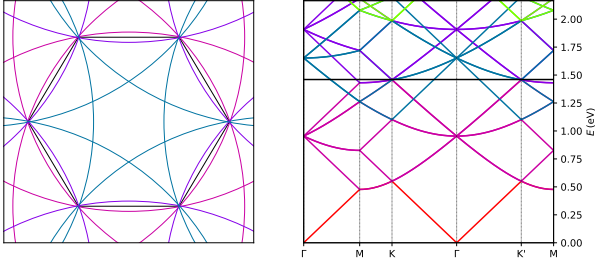


Figure S6. Diffraction orders of the honeycomb lattice in the empty lattice description, right along the high symmetry point lines, and left a crosscut at the energy of the K -point of interest in this manuscript. The colors denote different diffracted orders: red for the 0th, fuchsia for the 1st, navy blue for the 2nd, purple for the 3rd and green for the 4th.

electric field $\mathbf{E}_s(\mathbf{r}')$ at spot \mathbf{r}' of the image plane, where

$$\mathbf{E}_s(\mathbf{r}') \propto \mathbf{p}_s \frac{J_1(\alpha|\mathbf{r}' - \mathbf{R}'_s|)}{\alpha|\mathbf{r}' - \mathbf{R}'_s|}, \quad (\text{S1})$$

\mathbf{p}_s being the nanoparticle electric dipole moment, \mathbf{R}'_s the position of the particle image centre, α an inverse-length parameter depending on the setup, and J_1 the first order regular Bessel function. When multiple sources are present, their diffraction patterns will interfere with each other. Their respective electric field contributions are summed up, giving the resulting intensity at the image plane $I(\mathbf{r}') \propto |\sum_s \mathbf{E}_s(\mathbf{r}')|$. This is how we obtained the predicted patterns in Fig. 5 of the main text, as well as those mentioned here below. The exact choice of parameter α does not qualitatively affect the predicted patterns inside the array as long as the distance between image centres of two neighboring particles $|\mathbf{R}'_{s_1} - \mathbf{R}'_{s_2}|$ is well below the radius of first Airy disk minimum $\approx 1.22/\alpha$ (i.e. if the central circles of the Airy patterns of neighboring particles overlap), nor are the predicted array patterns qualitatively changed if the Airy functions are replaced with Gaussian disks.

The profiles of the measured diffraction patterns will differ from the ideal Airy or Gaussian patterns (de-

pending on the setup and optical components used) and are not exactly known, but the respective measured/predicted array patterns will match at the scale of several unit cells. At larger scales, however, the total optical path between the source nanoparticles and their corresponding image locations on the CCD will differ for different parts of the array, causing additional phase shifts in the observed patterns throughout the array.

A. Large-scale real-space images

In Fig. S7 we show the same pictures as in Fig. 5 of the main text, but over a larger area (right column) and also covering the whole sample (left column). The experimentally measured interference patterns extend over the whole sample size. But the observed pattern sometimes varies throughout the array; our hypothesis is that this is mainly due to the phase shifts depending on the construction of the measurement system as described above. However, any conclusions on this will require further study.

B. Comparison of real-space images for different eigenstates

Fig. S8 displays a set of measured real space intensity profiles for different polarization filter orientations, together with the predicted intensity patterns for the two singlets A'_1 and A'_2 , as well as for the doublet E' , with certain superpositions of the doublet states. The relative phases of the K and K' point lasing modes in the A'_1 and A'_2 columns are uncorrelated. These pictures demonstrate that, by inspecting the real space images for multiple values of the emission detection polarizer filter angle, one can distinguish a certain mode (here the singlet A'_1) from the other singlet as well as from a combination of the doublet states. While a single polarizer filter angle result would leave ambiguity between certain states, a tomographic polarization analysis using multiple angles leads to unambiguous results: for instance, the A'_1 and the first doublet combination produce somewhat similar image for the polarizer angle $-\pi/2$, but clearly distinct results for the angle $\pi/3$. These images also show that random, uncorrelated phases between the K and K' lasing contributions do not produce the precise pattern observed experimentally: sometimes, a match is found when assuming a constant relative phase between them, as shown in Fig. S9 and Fig. 5 of the main text.

C. Phase dependence of the real-space patterns

Fig. S9 shows how the simulated interference patterns evolve when the relative phase between the K - and K' -point lasing contributions vary. The situation where the

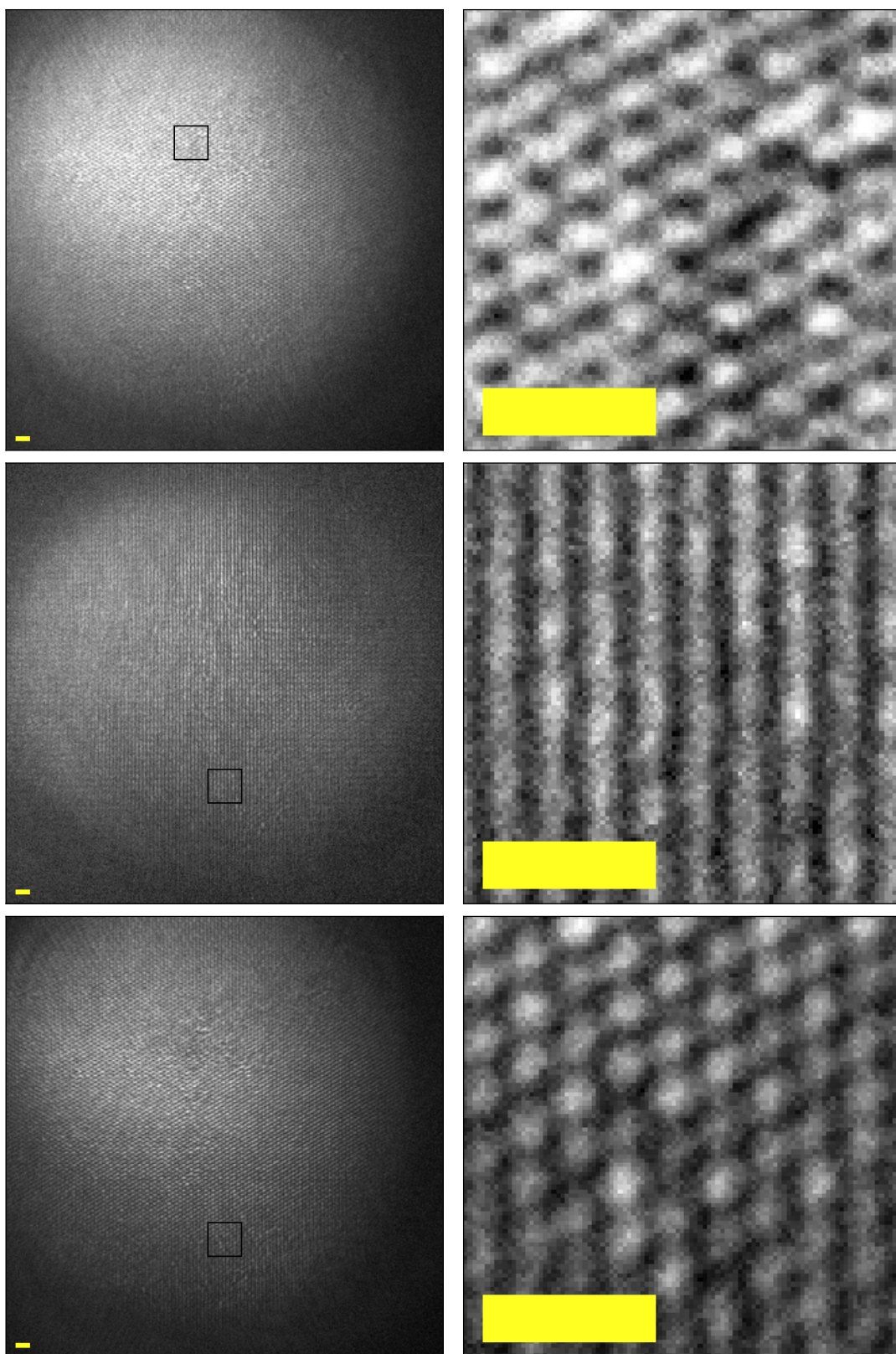


Figure S7. Left: real space image of the sample. Right: An enlarged image of the position marked by a square in the corresponding image on left. The images are for different polarization filters, top: no filter, middle: horizontal filter, bottom: vertical filter. The scalebars are $3 \mu\text{m}$ long.

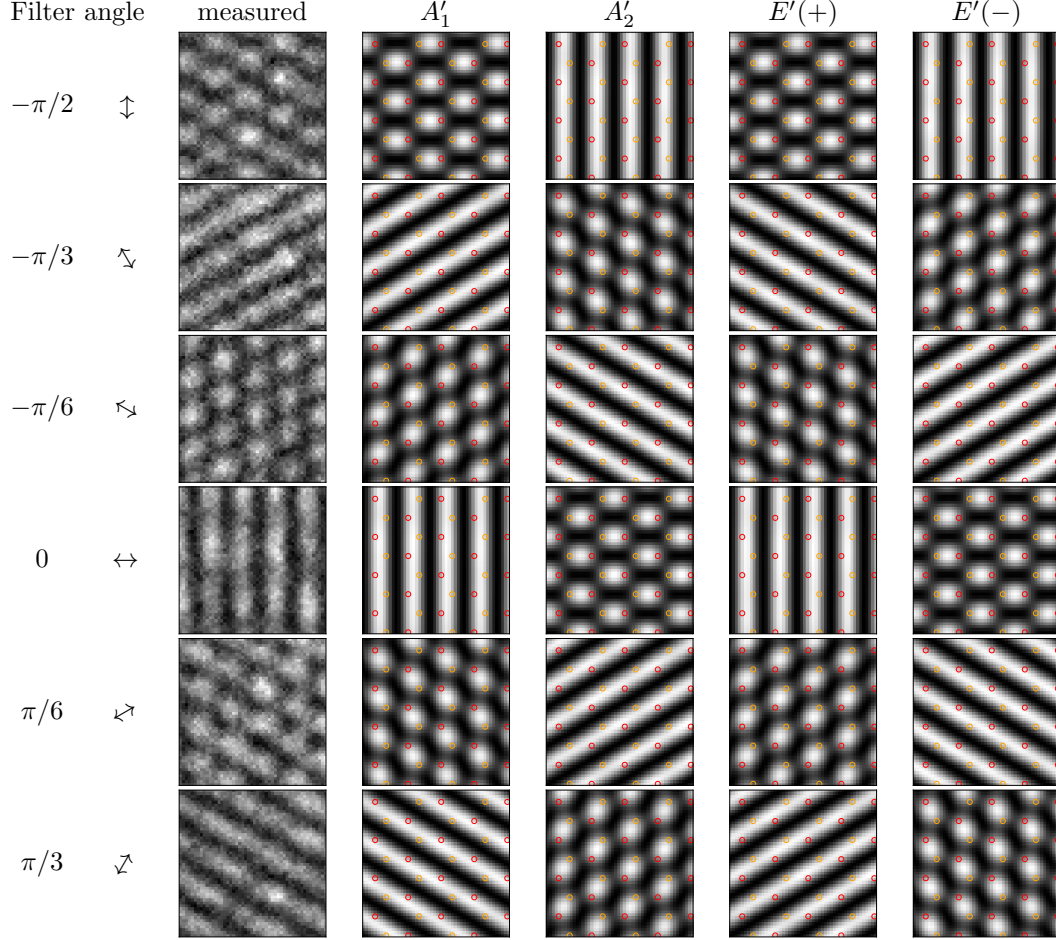


Figure S8. Comparison of measured real space patterns (left column) with the theoretically predicted patterns for various eigenstate choices (the rest of the columns), for different output emission polarization filter angles. Here the angle zero corresponds to the horizontal polarization filter in Fig. S7 and Fig. S9, and in Fig. 5 of the main manuscript. The theoretical predictions are for the singlets A'_1 and A'_2 (with uncorrelated phase between the K and K' contributions in both cases), and for the doublet state E' , for two different choices of the superposition phase between the doublet states (sum and difference, respectively, of the two doublet states depicted in Fig. 2(a) in the main text).

relative phase is random produces distinctly different interference patterns. These results demonstrate that the interference patterns can serve as accurate probe of not only the lasing modes involved but also of their relative phases.

IV. *T*-MATRIX SIMULATIONS

In order to get more detailed insight into the mode structure of the lattice around the lasing *K*-point – most importantly, how much do the mode frequencies at the *K*-points differ from the empty lattice model – we performed multiple-scattering *T*-matrix simulations [S5] for an infinite lattice based on our systems' geometry. We give a brief overview of this method in the subsections IV A, IV B below. The top advantage of the multiple-scattering *T*-matrix approach is its computational efficiency for large finite systems of nanoparticles. In the lattice mode analysis in this work, however, we use it here for another reason, specifically the relative ease of describing symmetries [S6].

Fig. S10(i) shows the dispersions around the *K*-point for the cylindrical nanoparticles used in our experiment. The *T*-matrix of a single cylindrical nanoparticle was computed using the scuff-tmatrix application from the SCUFF-EM suite [S7, S8] and the system was solved up to the $l_{\max} = 3$ (octupolar) degree of electric and magnetic spherical multipole. For comparison, Fig. S10(ii) shows the dispersions for a system where the cylindrical nanoparticles were replaced with spherical ones with radius of 45.4 nm, whose *T*-matrix was calculated semi-analytically using the Lorenz-Mie theory. In both cases, we used gold with interpolated tabulated values of refraction index [S9] for the nanoparticles and constant refraction index of 1.52 for the background medium. In both cases, the diffracted orders do split into separate bands according to the *K*-point irreducible representations (cf. section V), but the splitting is weak – not exceeding 2 meV for the spherical and 15 meV (3.2 meV for the *E*-in-plane modes) for the cylindrical nanoparticles. The splitting between A'_1 and A'_2 is very small; Fig. S11 shows a detail from Fig. 2(e) on a scale that enables to distinguish them.

A. The multiple-scattering problem

In the *T*-matrix approach, scattering properties of single nanoparticles in a homogeneous medium are first computed in terms of vector spherical wavefunctions (VSWFs)—the field incident onto the *n*-th nanoparticle from external sources can be expanded as

$$\mathbf{E}_n^{\text{inc}}(\mathbf{r}) = \sum_{l=1}^{\infty} \sum_{m=-l}^{+l} \sum_{t=\text{E,M}} p_n^{l,m,t} \mathbf{u}_{l,m}^t(\mathbf{r}_n) \quad (\text{S2})$$

where $\mathbf{r}_n = \mathbf{r} - \mathbf{R}_n$, \mathbf{R}_n being the position of the centre of *n*-th nanoparticle and $\mathbf{u}_{l,m}^t$ are the regular VSWFs which can be expressed in terms of regular spherical Bessel functions of $j_k(|\mathbf{r}_n|)$ and spherical harmonics $Y_{k,m}(\hat{\mathbf{r}}_n)$; the expressions, together with a proof that the VSWFs span all the solutions of vector Helmholtz equation around the particle, justifying the expansion, can be found e.g. in [S10, chapter 7] (care must be taken because of varying normalisation and phase conventions). On the other hand, the field scattered by the particle can be (outside the particle's circumscribing sphere) expanded in terms of singular VSWFs $\mathbf{v}_{l,m}^t$ which differ from the regular ones by regular spherical Bessel functions being replaced with spherical Hankel functions $h_k^{(1)}(|\mathbf{r}_n|)$,

$$\mathbf{E}_n^{\text{scat}}(\mathbf{r}) = \sum_{l,m,t} a_n^{l,m,t} \mathbf{v}_{l,m}^t(\mathbf{r}_n). \quad (\text{S3})$$

The expansion coefficients $a_n^{l,m,t}$, $t = \text{E, M}$ are related to the electric and magnetic multipole polarization amplitudes of the nanoparticle.

At a given frequency, assuming the system is linear, the relation between the expansion coefficients in the VSWF bases is given by the so-called *T*-matrix,

$$a_n^{l,m,t} = \sum_{l',m',t'} T_n^{lmt;l'm't'} p_n^{l',m',t'}. \quad (\text{S4})$$

The *T*-matrix is given by the shape and composition of the particle and fully describes its scattering properties. In theory it is infinite-dimensional, but in practice (at least for subwavelength nanoparticles) its elements drop very quickly to negligible values with growing degree indices l, l' , enabling to take into account only the elements up to some finite degree, $l, l' \leq l_{\max}$. The *T*-matrix can be calculated numerically using various methods; here we used the scuff-tmatrix tool from the SCUFF-EM suite [S7, S8], which implements the boundary element method (BEM).

The singular VSWFs originating at \mathbf{R}_n can be then re-expanded around another origin (nanoparticle location) $\mathbf{R}_{n'}$ in terms of regular VSWFs,

$$\mathbf{v}_{l,m}^t(\mathbf{r}_n) = \sum_{l',m',t'} S^{l'm't';lmt}(\mathbf{R}_{n'} - \mathbf{R}_n) \mathbf{u}_{l',m'}^{t'}(\mathbf{r}_{n'}), \quad |\mathbf{r}_n| < |\mathbf{R}_{n'} - \mathbf{R}_n|. \quad (\text{S5})$$

Analytical expressions for the translation operator $S^{l'm't';lmt}(\mathbf{R}_{n'} - \mathbf{R}_n)$ can be found in [S11].

If we write the field incident onto the *n*-th nanoparticle as the sum of fields scattered from all the other nanoparticles and an external field \mathbf{E}_0 (which we also expand around each nanoparticle, $\mathbf{E}_0(\mathbf{r}) = \sum_{l,m,t} p_{\text{ext}(n)}^{l,m,t} \mathbf{u}_{l,m}^t(\mathbf{r}_n)$),

$$\mathbf{E}_n^{\text{inc}}(\mathbf{r}) = \mathbf{E}_0(\mathbf{r}) + \sum_{n' \neq n} \mathbf{E}_{n'}^{\text{scat}}(\mathbf{r})$$

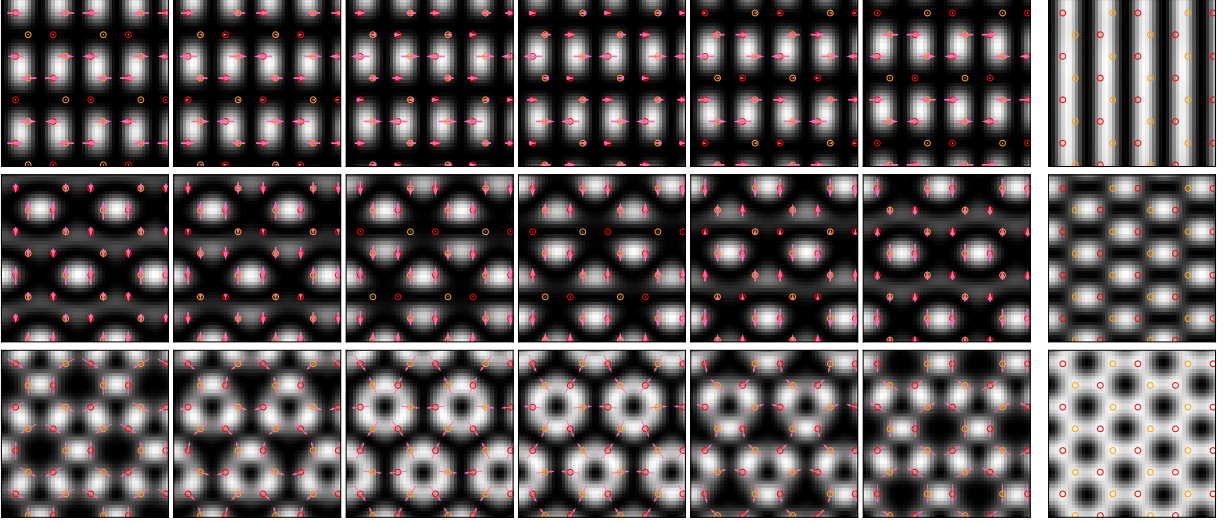


Figure S9. Dependence of the real-space patterns on the relative phase of the K and K' point realisations of the A'_1 mode. From top to bottom: horizontal filter, vertical filter, unfiltered. The sequences on the left depict the evolution of the real space pattern if the relative phase is shifted up to $\pi/3$. The patterns on the right correspond to the averaged intensity if the relative phase is totally random (or if only one of the K and K' -modes contribute).

and use eqs. (S2)–(S5), we obtain a set of linear equations for the electromagnetic response (multiple scattering) of the whole set of nanoparticles,

$$p_n^{l,m,t} = p_{\text{ext}(n)}^{l,m,t} + \sum_{n' \neq n} \sum_{l',m',t'} S^{lmt;l'm't'} (\mathbf{R}_n - \mathbf{R}_{n'}) \times \sum_{l'',m'',t''} T_{n'}^{l'm't';l''m''t''} p_{n'}^{l'',m'',t''}. \quad (\text{S6})$$

It is practical to get rid of the VSWF indices, rewriting (S6) in a per-particle matrix form

$$p_n = p_{\text{ext}(n)} + \sum_{n' \neq n} S_{n,n'} T_{n'} p_{n'} \quad (\text{S7})$$

and to reformulate the problem using (S4) in terms of the a -coefficients which describe the multipole excitations of the particles

$$a_n - T_n \sum_{n' \neq n} S_{n,n'} a_{n'} = T_n p_{\text{ext}(n)}. \quad (\text{S8})$$

Knowing $T_n, S_{n,n'}, p_{\text{ext}(n)}$, the nanoparticle excitations a_n can be solved by standard linear algebra methods. The total scattered field anywhere outside the particles' circumscribing spheres is then obtained by summing the contributions (S3) from all particles.

B. Periodic systems and mode analysis

In an infinite periodic array of nanoparticles, the excitations of the nanoparticles take the quasiperiodic Bloch-

wave form

$$a_{i\nu} = e^{i\mathbf{k} \cdot \mathbf{R}_i} a_\nu$$

(assuming the incident external field has the same periodicity, $p_{\text{ext}(i\nu)} = e^{i\mathbf{k} \cdot \mathbf{R}_i} p_{\text{ext}(\nu)}$) where ν is the index of a particle inside one unit cell and $\mathbf{R}_i, \mathbf{R}_{i'} \in \Lambda$ are the lattice vectors corresponding to the sites (labeled by multiindices i, i') of a Bravais lattice Λ . The multiple-scattering problem (S8) then takes the form

$$a_{i\nu} - T_\nu \sum_{(i',\nu') \neq (i,\nu)} S_{i\nu,i'\nu'} e^{i\mathbf{k} \cdot (\mathbf{R}_{i'} - \mathbf{R}_i)} a_{i'\nu'} = T_\nu p_{\text{ext}(i\nu)}$$

or, labeling $W_{\nu\nu'} = \sum_{i';(i',\nu') \neq (i,\nu)} S_{i\nu,i'\nu'} e^{i\mathbf{k} \cdot (\mathbf{R}_{i'} - \mathbf{R}_i)} = \sum_{i';(i',\nu') \neq (0,\nu)} S_{0\nu,i'\nu'} e^{i\mathbf{k} \cdot \mathbf{R}_{i'}}$ and using the quasiperiodicity,

$$\sum_{\nu'} (\delta_{\nu\nu'} \mathbb{I} - T_\nu W_{\nu\nu'}) a_{\nu'} = T_\nu p_{\text{ext}(\nu)}, \quad (\text{S9})$$

which reduces the linear problem (S8) to interactions between particles inside single unit cell. A problematic part is the evaluation of the translation operator lattice sums $W_{\nu\nu'}$; this is performed using exponentially convergent Ewald-type representations [S12].

In an infinite periodic system, a nonlossy mode supports itself without external driving, i.e. such mode is described by excitation coefficients a_ν that satisfy eq. (S9) with zero right-hand side. That can happen if the block matrix

$$M(\omega, \mathbf{k}) = \{\delta_{\nu\nu'} \mathbb{I} - T_\nu(\omega) W_{\nu\nu'}(\omega, \mathbf{k})\}_{\nu\nu'} \quad (\text{S10})$$

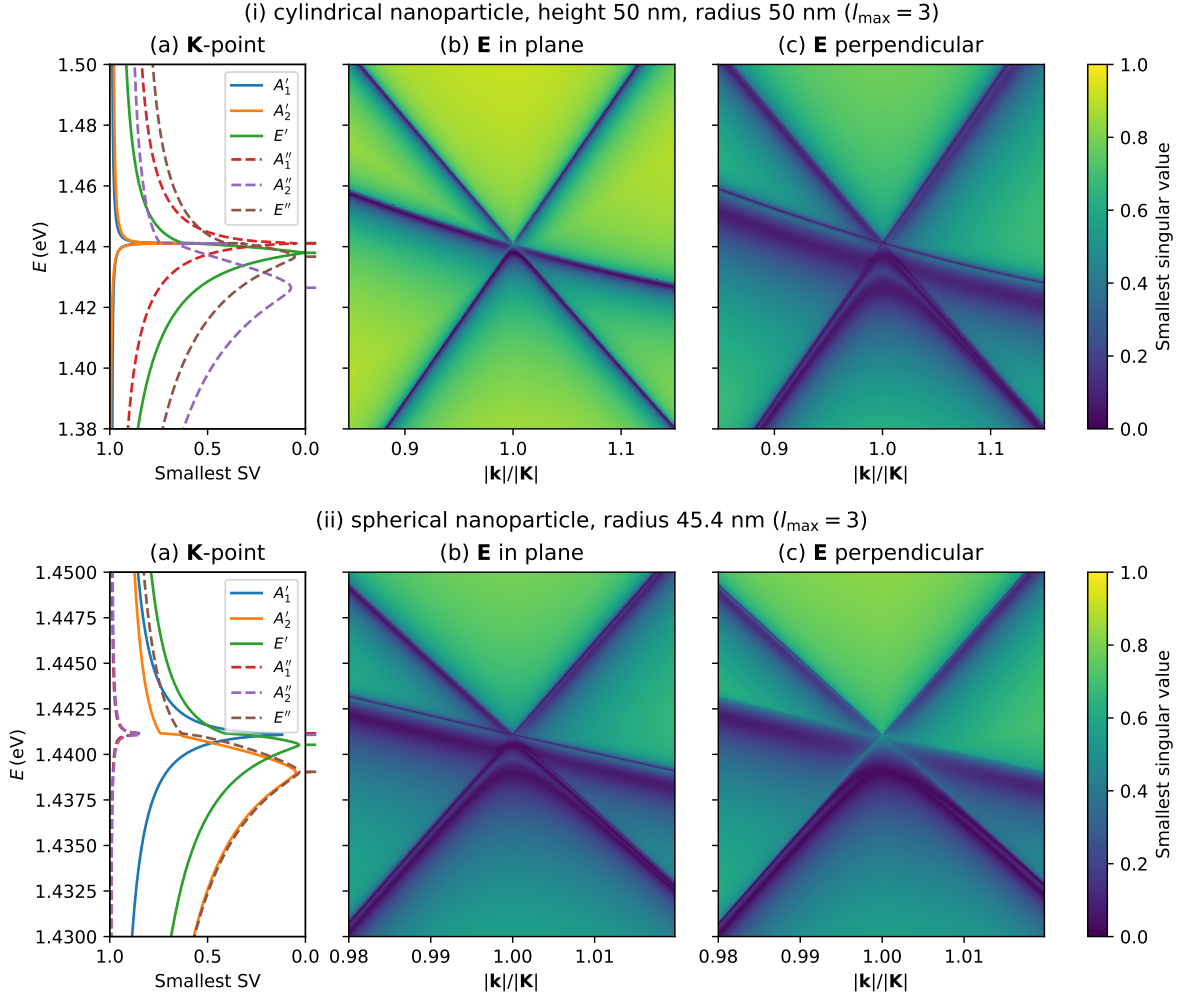


Figure S10. Band structure of infinite arrays around the K -point obtained using the T -matrix approach, with (i) T -matrix for a cylindrical nanoparticle (height 50 nm, radius 50 nm) computed with BEM, and (ii) T -matrix for a spherical nanoparticle (radius 45.4 nm) calculated using Lorenz-Mie theory. The lowest singular value (SV) of (S10) as a function of (ω, \mathbf{k}) is shown (a) exactly at the K -point for each irrep separately, (b) for \mathbf{E} -in-plane modes, and (c) for \mathbf{H} -in-plane modes.

from the left hand side of (S9) is singular (here we explicitly note the ω, \mathbf{k} dependence).

For lossy nanoparticles, however, perfect propagating modes will not exist and $M(\omega, \mathbf{k})$ will never be perfectly singular. Therefore in practice, we get the bands by scanning over ω, \mathbf{k} to search for $M(\omega, \mathbf{k})$ which have an "almost zero" singular value.

V. SYMMETRIES

A general overview of utilizing group theory to find lattice modes at high-symmetry points of the Brillouin zone can be found e.g. in [S3, chapters 10–11]; here we use the same notation.

We analyse the symmetries of the system in the same VSWF representation as used in the T -matrix formalism introduced above. We are interested in the modes at the

K -point of the hexagonal lattice, which has the D_{3h} point symmetry. The six irreducible representations (irreps) of the D_{3h} group are known and are available in the literature in their explicit forms. In order to find and classify the modes, we need to find a decomposition of the lattice mode representation $\Gamma_{\text{lat.mod.}} = \Gamma^{\text{equiv.}} \otimes \Gamma_{\text{vec.}}$ into the irreps of D_{3h} . The equivalence representation $\Gamma^{\text{equiv.}}$ is the E' representation as can be deduced from [S3, eq. (11.19)], eq. (11.19) and the character table for D_{3h} . $\Gamma_{\text{vec.}}$ operates on a space spanned by the VSWFs around each nanoparticle in the unit cell (the effects of point group operations on VSWFs are described in [S6]). This space can be then decomposed into invariant subspaces of the D_{3h} using the projectors $\hat{P}_{ab}^{(\Gamma)}$ defined by [S3, eq. (4.28)]. This way, we obtain a symmetry adapted basis $\{\mathbf{b}_{\Gamma,r,i}^{\text{s.a.b.}}\}$ as linear combinations of VSWFs $\mathbf{v}_{l,m}^{p,t}$ around

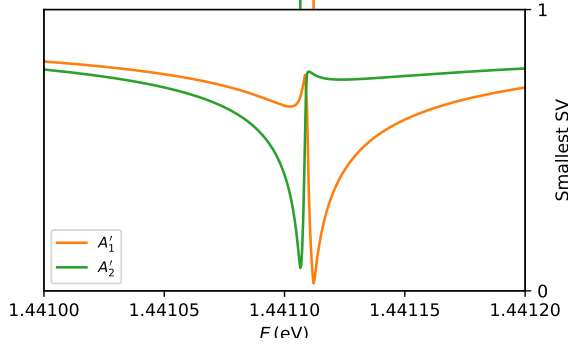


Figure S11. The lowest singular values of (S10) exactly at the K -point, in the A_1' and A_2' subspaces for the cylindrical nanoparticle. The data are the same as in Figs. 2(e) and S10(i)(a), but plotted on a scale that enables to distinguish between the two curves.

the constituting nanoparticles (labeled p),

$$\mathbf{b}_{\Gamma,r,i}^{\text{s.a.b.}} = \sum_{l,m,p,t} U_{\Gamma,r,i}^{p,t,l,m} \mathbf{v}_{l,m}^{p,t}$$

where Γ stands for one of the six different irreps of D_{3h} , r labels the different realisations of the same irrep, and the last index i going from 1 to d_Γ (the dimensionality of Γ) labels the different partners of the same given irrep. The number of how many times is each irrep contained in $\Gamma_{\text{lat.mod}}$. (i.e. the range of index r for given Γ) depends on the multipole degree cutoff l_{max} .

Each mode at the K -point shall lie in the irreducible spaces of only one of the six possible irreps and it can be shown via [S3, eq. (2.51)] that, at the K -point, the matrix $M(\omega, \mathbf{k})$ defined above takes a block-diagonal form in the symmetry-adapted basis,

$$M(\omega, \mathbf{K})_{\Gamma,r,i;\Gamma',r',j}^{\text{s.a.b.}} = \frac{\delta_{\Gamma\Gamma'}\delta_{ij}}{d_\Gamma} \sum_q M(\omega, \mathbf{K})_{\Gamma,r,q;\Gamma',r',q}^{\text{s.a.b.}}$$

This enables us to decompose the matrix according to the irreps and to solve the singular value problem in each irrep separately, as done in Fig. S10(a).

-
- [S1] J. Thompson, M. Anni, S. Lattante, D. Pisignano, R. Blyth, G. Gigli, and R. Cingolani, *Synth. Met.* **143**, 305 (2004).
- [S2] T. K. Hakala, A. J. Moilanen, A. I. Väkeväinen, R. Guo, J.-P. Martikainen, K. S. Daskalakis, H. T. Rekola, A. Julku, and P. Törmä, *Nat. Phys.* **14**, 739 (2018).
- [S3] M. S. Dresselhaus, G. Dresselhaus, and A. Jorio, *Group Theory: Application to the Physics of Condensed Matter* (Springer, Berlin, Heidelberg, 2008).
- [S4] J. D. Dixon, *Math. Comp.* **24**, 707 (1970).
- [S5] D. W. Mackowski, *Proc. R. Soc. London, Ser. A* **433**, 599 (1991).
- [S6] F. M. Schulz, K. Stamnes, and J. J. Stamnes, *J. Opt. Soc. Am. A* **16**, 853 (1999).
- [S7] H. Reid, “SCUFF-EM,” (2018), <http://github.com/homerreid/scuff-EM>.
- [S8] M. T. H. Reid and S. G. Johnson, *IEEE Trans. Antennas Propag.* **63**, 3588 (2015), arXiv:1307.2966.
- [S9] P. B. Johnson and R. W. Christy, *Phys. Rev. B* **6**, 4370 (1972).
- [S10] G. Kristensson, *Scattering of Electromagnetic Waves by Obstacles* (SciTech Publishing, Edison, NJ, 2016).
- [S11] Y.-l. Xu, *J. Comput. Phys.* **139**, 137 (1998).
- [S12] C. Linton, *SIAM Rev.* **52**, 630 (2010).